

OBSCURATION AND ORIGIN OF NUCLEAR X-RAY EMISSION
IN FR I RADIO GALAXIES

D. DONATO

George Mason University, School of Computational Sciences, 4400 University Drive, Fairfax, VA 22030

AND

R. M. SAMBRUNA AND M. GLIOZZI

George Mason University, Dept. of Physics & Astronomy and School of Computational Sciences, MS 3F3,
4400 University Drive, Fairfax, VA 22030*Draft version May 27, 2018*

ABSTRACT

We present X-ray observations of the nuclear region of 25 Fanaroff-Riley I radio galaxies from the 3CRR and B2 catalogs, using data from the *Chandra* and *XMM* archives. We find the presence of a X-ray Central Compact Core (CCCX) in 13/25 sources, in 3/25 sources the detection of a CCCX is uncertain, while in the remaining 9/25 sources no CCCX is found. All the sources are embedded in a diffuse soft X-ray component, generally on kpc-scales, which is in agreement with the halo of the host galaxy and/or with the intracluster medium. The X-ray spectra of the cores are described by a power law with photon indices $\Gamma = 1.1 - 2.6$. In 8 sources excess absorption over the Galactic value is detected, with rest-frame column densities $N_H^z \sim 10^{20} - 10^{21} \text{ cm}^{-2}$; thus, we confirm the previous claim based on optical data that most FRI radio galaxies lack a standard optically-thick torus. We find significant correlations between the X-ray core luminosity and the radio and optical luminosities, suggesting that at least a fraction of the X-ray emission originates in a jet; however, the origin of the X-rays remains ambiguous. If the X-ray emission is entirely attributed to an isotropic, accretion-related component, we find very small Eddington ratios, $L_{bol}/L_{Edd} \sim 10^{-3} - 10^{-8}$, and we calculate the radiative efficiency to be $\eta \sim 10^{-2} - 10^{-6}$, based on the Bondi accretion rates from the spatial analysis. This suggests that radiatively inefficient accretion flows are present in the cores of low-power radio galaxies.

Subject headings: Galaxies: active – Galaxies: fundamental parameters – Galaxies: nuclei – X-rays: galaxies

1. INTRODUCTION

According to unification schemes, radio galaxies are the mis-oriented parent population of jet-dominated blazars, and thus correspond to large viewing angles to the jet/torus axes. The low-power ($P_{178 \text{ MHz}} \lesssim 2 \times 10^{25} \text{ erg s}^{-1}$), centrally-brightened Fanaroff-Riley I (FRI) galaxies are the misaligned versions of BL Lac objects, while high-power, edge-brightened FRIIs are unified with powerful quasars. Thus, if the unification models for radio-loud sources hold, emission from the cores of both FRIs and FRIIs should be significantly obscured by dust and gas contained by the torus. Moreover, the accretion flow could be different at high and low-powers, with FRIIs being powered by a standard disk and FRIs by an ADAF (Reynolds et al. 1996; Ghisellini & Celotti 2001). These questions bear significance to the origin of the FRI/II dichotomy.

While observations from optical to X-rays of FRIIs support the presence of an obscuring dusty torus in these sources (Sambruna, Eracleous, & Mushotzky 1999; Chiaberge, Capetti, & Celotti 2000), its presence in FRIs is still highly controversial. Optical *HST* images of FRIs show that in most of these galaxies an unresolved nuclear point source is present (Chiaberge, Capetti, & Celotti 1999; Capetti et al. 2002, hereafter CH99 and CA02) arguing for lack of obscuration along the line of sight. The optical flux correlates tightly with the radio core flux, suggesting a non-thermal (synchrotron) origin of the optical emission from the base of the jet (CH99). However, using

the same optical and radio data, Cao & Rawlings (2004) concluded that in most of the cases the emission from the central engine of FRIs is heavily obscured and is produced by a standard accretion disk.

At X-rays, FRIs were previously observed with *ROSAT* and *ASCA*. The *ROSAT* observations showed that the cores are embedded in diffuse soft X-ray emission associated to the galaxy's ISM. The core X-ray flux correlates with the radio flux, suggesting a jet origin for the X-ray emission (Hardcastle & Worrall 2000). However, a correlation between X-ray and radio fluxes may ensue from a more general correlation (fundamental plane in 3-D space) between black hole mass, X-ray, and radio emission, where the radio is produced by the jet whereas the X-rays are related to the accretion flow (Merloni, Heinz, & di Matteo 2003). At energies above 2 keV, the *ASCA* spectra of 7 FRIs are best described by a power-law component with photon index $\Gamma \sim 1.3 - 1.9$ (Sambruna, Eracleous, & Mushotzky 1999). Due to the large PSF of the *ASCA* detectors, however, contributions from off-nuclear X-ray point sources cannot be excluded (e.g., Turner et al. 1997).

The combination of *XMM-Newton* (or simply *XMM*) and *Chandra*, with their complementary capabilities, is ideal to study these complex X-ray sources and address, in particular, the issue of nuclear obscuration. The unprecedented spatial resolution of *Chandra* allows one to disentangle the different components (unresolved core, kpc jet, point like sources, diffuse emission) contributing to the X-ray emission. Moreover, with *Chandra* one can in-

investigate directly the circumnuclear region, measuring the density and temperature profiles close to the accretion radius of the central black hole. On the other hand, the larger effective area of *XMM* and the combination of the EPIC cameras working simultaneously results in a superior photon yield, which allows more detailed analysis of the nuclear X-ray spectrum. A further advantage of *XMM* is that also bright point-like sources are not affected by pile-up problems, which is unfortunately common in *Chandra* observations. In fact, the advantage of the complementary use of *XMM* and *Chandra* was demonstrated in a previous study of the FRI 3C 270 (Gliozzi, Sambruna, & Brandt 2003).

Here we extend this study to archival FRIs in order to test the unification models and the origin of the FRI/II division. The basic questions we will address are: i) Do FRIs have obscuring tori? Does the column density correlate with luminosity, inclination angle? ii) What is the origin of the nuclear X-ray emission? How much does the beamed component contribute to the nuclear X-ray flux? If the X-rays originate from the accretion flow, iii) What is the nature of accretion in the nuclei of FRIs?

The outline of the paper is as follows. In § 2 we discuss the sample selection criteria and in § 3 the observations and data analysis. Results of the spatial and spectral analysis are given in § 4. Correlations between parameters are presented in § 5, while the interpretation of the results is given in § 6. Throughout this paper, $H_0 = 75 \text{ km s}^{-1} \text{ Mpc}^{-1}$ and $q_0 = 0.5$ are adopted.

2. SAMPLE AND X-RAY OBSERVATIONS

We started with the samples presented in CH99 and CA02. Chiaberge’s sample contains 33 radio galaxies belonging to the 3CR catalog (Spinrad et al. 1985) and morphologically identified as FR I radio sources by Laing, Riley, & Longair (1983) and/or Zirbel & Baum (1995). Capetti’s sample, on the other hands, contains 57 radio galaxies belonging to the B2 catalog (Colla et al. 1975; Fanti et al. 1978). These samples contain all the *bona fide* FRI radio galaxies observed in the optical with *HST*.

We cross-correlated the CH99 and CA02 samples with the *Chandra* and *XMM* archives, and selected all the sources with available X-ray observations up to January 2004. The final sample, which contains 25 sources, is reported in Table 1. Also listed are redshifts, radio, optical, and UV luminosities from CH99 and CA02. The inclination angles of the radio jet with respect to the line of sight in column 5 were obtained from the literature, listed in column 6. The inclination angles are usually determined from high resolution radio data using the brightness ratio between the parsec-scale jet and the counter-jet, and/or the arcsecond scale core dominance with respect to the total power of the source (e.g., Giovannini et al. 2001). Unfortunately, for many sources no uncertainties are reported in the literature. Column 7 lists the mass of the central black hole, derived from the correlation between the stellar velocity dispersion of the host bulge and its B-band magnitude (Marchesini, Celotti, & Ferrarese 2004).

Among the 25 sources available in the *Chandra* and *XMM* archives, 11 have only *Chandra* observations (1 source with ACIS-I and 10 with ACIS-S), 3 have only *XMM* observations, and the remaining 11 have been ob-

served with both satellites. For the sources with both *Chandra* and *XMM* observations, the former satellite has been used for the spatial analysis (except for 3C 84 which is affected by severe pile-up). Also, for the spectral analysis *Chandra* observations have been preferred because of the ability to disentangle the nuclear from the diffuse component; however, in 4 cases (B2 0120+33, B2 0149+35, 3C 274.0, and 3C 338) *XMM* observations have been used due to the poor *Chandra* spectra.

The log of the X-ray observations is reported in Table 2.

3. X-RAY OBSERVATIONS AND DATA REDUCTION

3.1. *Chandra*

The *Chandra* observations were carried out between 2000 April and 2004 January. All were performed with ACIS-S, with the sources at the nominal aimpoint of the S3 chip, except for 3C 28 which was observed with ACIS-I. In several cases, the original observers requested a reduced frame time to mitigate core pile-up. In the case of 3C 78, no reduced time frame was requested for the short *Chandra* observations and the core suffers from significant pileup (28%). No spatial or spectral analysis was performed for this object. The ACIS event files were screened using CIAO 2.3 according to standard criteria.

Background spectra and light curves were extracted from source-free regions on the same chip of the source. Time intervals corresponding to background flares were excluded. The net exposure times are listed in Table 2. Spectra were extracted from a circular region with radius $1.5''$ (see § 4.1), and their response matrices were constructed using the corresponding thread in CIAO 2.3. The ACIS spectra were analyzed in the energy range 0.3–8 keV, where the calibration is best known and the background negligible.

3.2. *XMM-Newton*

Given that the cores of FRIs are relatively weak X-ray emitters, we used only data from the EPIC pn and MOS cameras for our analysis. These were performed using different observing modes (extended and full frame) and different filters (thin and medium), as specified by the original observers.

No core pile-up was detected in either the pn or MOS cameras according to the SAS task `epatplot`. The recorded events were screened to remove known hot pixels and other data flagged as bad. For *XMM*, only data with `FLAG=0` were used. The data were processed using the latest CCD gain values, and only events corresponding to pattern 0–12 (singles, doubles, triples, and quadruples) in the MOS cameras and 0–4 (singles and doubles only, since the pn pixels are larger) in the pn camera were accepted. Arf and rmf files were created with the *XMM* Science Analysis Software SAS5.4.

EPIC spectra were extracted in circular regions centered on the core and with radii $20''$ – $30''$, depending on the intensity and the location on the chip of the source. Spectral analysis was performed in the energy range 0.2–10 keV.

4. RESULTS

4.1. *Spatial Analysis*

Figure 1 and 2 show the *Chandra* and *XMM* images of the sources, with the soft X-ray contours in 0.3–2 keV overlaid on the hard X-ray (2–8 keV) images. Both soft and hard X-ray images were smoothed using the sub-package *fadapt* of *FTOOLS* with a circular top hat filter of adaptive size in order to achieve a minimal number of 10 counts under the filter. Inspection of Figure 1 and 2 shows the presence of diffuse soft X-ray emission in all sources. In most cases, the diffuse emission is on kpc-scales and is associated with the host galaxy halo. In 3C 28, B2 0120+33, B2 0149+35, 3C 84, 3C 272.1, B2 1346+26, 3C 317, and 3C 338 the soft X-rays appear to extend on larger, cluster-like scales. Hard X-ray point sources are present in several cases (see below). X-ray jets are present in B2 0055+30 (Worrall, Birkinshaw, & Hardcastle 2003), 3C 31 (Hardcastle et al. 2002), 3c 66B (Hardcastle, Birkinshaw, & Worrall 2001), B2 0755+37 (Worrall, Birkinshaw, & Hardcastle 2001), 3C270 (Chiaberge et al. 2003), and 3C274.0 (Marshall et al. 2002; Wilson & Yang 2002).

Since this paper focuses on the X-ray emission from the radio galaxy cores, it is important to know in how many cases an unresolved X-ray source is detected. To quantify this, we performed a detailed spatial analysis of the *Chandra* and *XMM* data.

We adopted the following procedure. First, radial surface-brightness profiles were extracted from a series of concentric annuli centered on the radio core position. Off-nucleus X-ray point sources, as well as the X-ray jet, were excluded. Second, the radial profiles were fitted with a model including the instrument Point Spread Function (PSF) and one or more β models to describe the diffuse soft X-ray emission. The significance of the PSF was determined using an F-test, assuming as threshold for significant detection of the PSF a probability $P_F = 99\%$, corresponding to a 3σ confidence level.

For the *XMM* images, the PSF was described using the analytical description of Ghizzardi (2001). Since the aimpoint of the EPIC-pn camera is very close to the edge of the CCD (limiting the extension of the extraction regions to few arcseconds), we decided to use only EPIC-MOS1 data. For the *Chandra* images, the PSF was created using the *Chandra* Ray Tracer (*ChaRT*) simulator which takes into account the spectral distribution of the source. The ACIS PSF was thus described using the 6-parameter function:

$$PSF(x) = A_0 e^{-A_1 x^{A_2}} + A_3 e^{-A_4 x^{A_5}}$$

where the free parameters were determined by fitting the radial profile of the PSF.

The β model is described by the following formula (e.g., Cavaliere & Fusco-Femiano 1976):

$$S(r) = S_0 \left(1 + \frac{r^2}{r_c^2} \right)^{-3\beta+1/2}.$$

Table 3 summarizes the X-ray core detections, while Table 4 lists the best-fit parameters (core radius, β value) for the β models. Three examples of the fit of radial profiles are shown in Figure 3.

Column 2 of Table 3 flags those FRIs where a Compact Central Core (CCC) was detected with *HST* in the optical. For analogy, we will use the term CCCX to indicate the CCC counterpart in the X-rays. As apparent from Table 3, a CCCX was detected in 13/25 sources, while no

CCCX is present in 9 sources. In the case of B2 2116+26, the PSF is significant at $P_F = 95.6\%$, corresponding to a 2σ confidence level. However, the *Chandra* observation is one of the shortest, with only 9.6 ks of live time. We regard this source as a likely CCCX candidate. The remaining 3 sources -3C 78, 3C 264, and 3C 272.1- are discussed here individually.

3C 78: due to the strong core pileup, which distorts the shape of the PSF, no reliable fit to the radial profiles could be performed. However, the presence of central pileup is *di per se* indication of strong unresolved X-ray emission. Therefore, we conclude that a CCCX is present in 3C 78.

3C 264: the PSF is dramatically distorted due to the large offset from nominal aimpoint of the source. Thus, no reliable spatial analysis can be performed. However, the source spectrum (see Table 5) shows the presence of a hard X-ray power-law component. We interpret this component as the signature of non-thermal emission from an AGN. We consider the detection of a CCCX uncertain in this case.

3C 272.1: the *Chandra* image shows soft X-ray emission with a very disturbed morphology. The radial profile cannot be properly fitted with β -model(s) since the spatial fit does not converge. As the inspection of the hard X-ray image shows the presence of a point source, conservatively we consider the CCCX detection uncertain.

Let us now compare the detection rate of the CCC and of the CCCX. We find that:

- Of the 18 FRIs with a CCC in the optical, 13 have also a CCCX;
- All FRIs with a detected CCCX have a detected CCC, except 3C 438;
- No compact core was detected at either optical or X-rays in 3 FRIs (3C 28, B2 0120+33, and B2 1257+28).

There are two possibilities for the non-detection of CCCX: either the AGN X-ray emission is intrinsically weak (below the detection threshold of *Chandra* or below the level of the circumnuclear extended emission), or it is absorbed by a very large amount of cold gas, $N_H^z > 10^{24} \text{ cm}^{-2}$. The first case will be discussed in § 4.3, while the second case in § 6.1.

4.2. Variability Analysis

We searched for X-ray flux variability in the background-subtracted light curves of the sources with positive CCCX detections. When possible, *XMM* data were used to take advantage of the larger signal-to-noise ratio of the EPIC data. According to a χ^2 test for constancy, no significant variability of the 2–10 keV flux is detected in the sources of our sample, except for 3C 270. For more details on this source we refer to Gliozzi, Sambruna, & Brandt (2003).

4.3. Spectral Analysis

The main goal of the X-ray spectral analysis is to investigate the physical conditions of the sources in the sample, focusing on the non-thermal emission from the 15 detected

CCCX. We also include the two CCCX candidates 3C 264 and 3C 272.1, while 3C 78 was not considered because of the strong core pileup problems.

The ACIS and EPIC spectra, extracted as described above (§ 3), were grouped so that each new bin had $\gtrsim 20$ counts to enable the use of the χ^2 statistics. For 3C 438, for which $\lesssim 200$ counts were detected, the X-ray spectrum was not rebinned and the C-statistic was used instead. The spectra were fitted within XSPEC v.11.2.0. Errors quoted throughout are 90% for one interesting parameter ($\Delta\chi^2=2.7$).

The X-ray spectra were fitted with a two-component model, both absorbed by Galactic N_H . At soft energies, the circumnuclear emission from the host galaxy and/or from the cluster was parameterized by a thermal component, the model `apex` in XSPEC, with temperature kT and abundance Z/Z_\odot . During the fits, the abundance was left free to vary between 0.2 and 1, or otherwise fixed at one of these two limits. For sources embedded in a galaxy cluster, often more than a single thermal component was requested to adequately fit the data, since the cluster can have a gradient of temperatures and/or abundances in the ACIS/EPIC extraction radii.

At hard X-rays, a power-law model with photon index Γ was used to describe the CCCX non-thermal emission. The power law is absorbed by a column density N_H^z at the redshift of the source, thus representing any excess intrinsic absorption over the Galactic value. We note that most CCCX are at low z , thus absorption by the ISM along the line of sight is likely not to be significant. The significance of the power-law component over the thermal model was determined with the F-test.

The results of the spectral fits are presented in Table 5. Three spectra are shown in Figure 4 corresponding to the 3 qualitatively different surface brightness shown in Figure 3. For all the sources with a detected CCC in the X-rays, the power-law component is always required at high significance level ($P_F \gtrsim 95\%$). For the sources without a CCCX, the power law is not requested and the X-ray spectrum is adequately described by one or multiple thermal components.

In 8 sources, statistically significant absorption over the Galactic value is detected, with $N_H^z \sim 10^{20} - 10^{21} \text{ cm}^{-2}$ (see also Figure 5). The source 3C 270 stands out for the largest intrinsic column density, $N_H^z \sim 10^{22} \text{ cm}^{-2}$, in agreement with previous findings (Gliozzi, Sambruna, & Brandt 2003). The power law photon index spans a wide range of values, $\Gamma \sim 1.1 - 2.6$, with average value $\langle \Gamma \rangle = 1.9$ and standard deviation $\sigma = 0.4$.

Most of the FRIs of the our sample are embedded in diffuse emission on the scale of the host galaxy halo, \sim several kpc (Table 4). The fitted temperatures are $kT \sim 0.3 - 1 \text{ keV}$, in agreement with previous results (Sambruna, Eracleous, & Mushotzky 1999; Worrall & Birkinshaw 2000).

The observed fluxes and intrinsic (absorption-corrected) luminosities in the energy range 0.3–8 keV are reported in Table 6. Also listed in the Table are the observed fluxes and intrinsic luminosities in 0.3–8 keV for the power law component only. The latter span 3 orders of magnitude, with $L_X \sim 10^{40} - 10^{43} \text{ erg s}^{-1}$. Comparing the values in Table 6, it is apparent that the AGN power-law emission

typically contributes $\gtrsim 50\%$ of the total X-ray emission. This result is independently confirmed by the analysis of the radial profiles: evaluating the integrated area under the PSF and under the β -model over the inner 20'' we find that the PSF-to-total flux ratio is $\gtrsim 50\%$.

In the cases of 3C 28, B2 0149+35, and B2 2116+26, no power-law component was required in the X-ray spectrum, in line with the fact that a CCCX is not detected in these sources. However, limits to the contribution of the X-ray emission due to the AGN can be derived from the radial profiles (e.g., Figure 3). While the PSF is not statistically significant, the normalization on the PSF can be used to calculate an upper limit on the relative AGN contribution to the total X-ray emission. We find that the AGN contributions are of the order of $\sim 6\%$, $\sim 1\%$, and $\sim 30\%$, respectively.

For the remaining 5 sources with undetected CCCX, we used the most conservative value of the ratio ($\sim 1\%$) to derive the upper limit on the AGN luminosity. The values are reported in part b) of Table 6.

5. CORRELATIONS

We have investigated possible trends among various parameters related to the core emission, namely, the X-ray, optical, and radio luminosities, the absorption column density, and the inclination angle of the radio jet. The goal is to uncover clues on the origin of the X-ray emission and on the presence of an obscuring torus, as expected in the context of unification models.

To quantify the degree of linear correlation, we calculated the linear correlation coefficient $|r|$ and computed the chance probability $P_r(N)$ that a random sample of N uncorrelated pairs of measurements would yield a linear correlation coefficient equal or larger than $|r|$. If the chance probability is small, the two quantities are likely to be correlated. We use as minimum probability of correlation $P_r(N) < 1\%$ (which corresponds to a 3σ level). To account for upper limits, we used the generalized Kendall's Tau test contained in the statistical package ASURV (Lavalley, Isobe, & Feigelson 1992). The chance probabilities and the linear correlation coefficients with the intercept coefficient and slope of the linear regression ($y=a+bx$) are shown in Table 7a for the detections and in Table 7b when limits are included.

Figure 6a shows the plot of the intrinsic column density N_H^z (Table 6) versus the inclination angle of the jet (Table 1). According to the unification schemes, the obscuring torus becomes more prominent for larger viewing angles, so we would expect a trend of larger N_H^z for larger angles. No such trend is present in Figure 6a, over 3 decades in N_H^z and a factor 4 in angle. We conclude that FRIs lack a standard thick obscuring torus, in contrast with the expectations from the unification models.

In Figure 6b, we show the plot of the intrinsic X-ray luminosity of the AGN versus the inclination angle of the radio jet. Formally, a linear regression analysis shows that there is no significant correlation. However, if the outliers sources 3C 338 and 3C 438 are excluded, a marginally significant correlation is detected, $P_r(N) = 2.3\%$. The correlation becomes statistically significant, $P_r(N) = 0.5\%$, if only the *Chandra* data (without 3C 438) are considered. The trend is in the sense of decreasing X-ray luminosity

with increasing angle, as expected if a fraction of the X-ray emission is anisotropic, for example related to a beamed component. Indeed, the X-ray luminosity also correlates tightly with the radio and optical luminosities (Figures 6c and 6d), for which an origin from the unresolved jet was argued (CH99; Hardcastle & Worrall 2000; CA02)

As for the outliers, we note that 3C 438 are classified as an FRI radio galaxy by CH99 but as an FRII by Rawlings et al. (1989): it is thus possible that this source is an intermediate FRI/II. In the case of 3C 338, the nucleus shows a high X-ray to submillimeter luminosity ratio compared to other 3C radio sources (Quillen, Almog, & Yukita 2003). Both sources can thus be considered “anomalous” in the present sample.

A label in Figure 6b marks the position of 3C 274.0 (M87) and 3C 270. The first source is interesting because it was argued recently on the basis of the *Chandra* data that the X-ray core flux originates from the base of the jet (Marshall et al. 2002); however, in the Figure 6b this source has a deficit of X-ray emission. Variability could possibly account for this discrepancy (Harris 2003). On the other hands, 3C 270 appears to have an excess of X-ray flux for its given inclination, supporting our previous claims that the bulk of the X-ray emission originates from the accretion flow (Gliozzi, Sambruna, & Brandt 2003).

It is worth noting that several issues can affect the angle-to- L_X correlation, as well as the angle-to- N_H^z correlation: a) uncertainties on the angles, which are rarely reported in the literature or are poorly determined. This is shown for example by a detailed study of VLBI observations of a complete sample of radio galaxies from the B2 and 3CR catalogs Giovannini et al. (2001), where the errors range from a few to dozens of degrees; b) beaming effects, which should not play an important role at relatively large angles; c) the possible concentration of obscuring material on the equatorial plane, which can cause an intrinsically isotropic emission to appear anisotropic. For these reasons the origin of the X-ray radiation, that is, the fraction of X-rays produced by the jet and by the accretion process, remains an open question.

6. DISCUSSION

6.1. Obscuration in FRIs

An intriguing result of this paper is the finding that FRIs have little or no excess X-ray absorption in their cores. This result fits into the current debate, sparked by recent optical results, of whether or not low-power radio galaxies have an obscuring pc-scale torus. As mentioned earlier, *HST* images showed the presence of a compact core in the majority of 3C and B2 FRIs (CH99, CA02). However, based on the same data, it was argued by Cao & Rawlings (2004) that a standard torus is indeed present in FRIs, obscuring most of the isotropic radiation from the nucleus, and that the detected unresolved optical core is the emission of the jet on scales of tens of parsec. The *Chandra* and *XMM* data support CH99 conclusions that no pc-scale torus is present in FRIs.

We now examine the possibility that the *direct* X-ray emission from the core is blocked by a Compton-thick torus ($N_H^z > 10^{24} \text{ cm}^{-2}$), and that the measured X-ray radiation is due to reflection toward the observer by a “mirror” located above the torus, as postulated for Seyfert 2 galax-

ies (e.g., Matt et al. 2000). In this case, the values of N_H^z in Table 5 would not be associated to the torus, and an alternative explanation would have to be found.

To test the Compton-thick torus hypothesis, we calculated for each source of our sample the ratio $T = L_X/L_{OIII}$, where L_X is the unabsorbed 2-10 keV luminosity of the CCCX and L_{OIII} is the dereddened O III luminosity from the literature. The latter is produced in the Narrow-Line Region and is considered a good indicator of the intrinsic AGN power. The average value for our FRI sample is $T_{\text{FRI}} = 34.4 \pm 8.0$, where the uncertainty is the standard dispersion. The average value of T for the FRIs of our sample was compared to the value derived for a sample of 9 Seyfert 1 galaxies and for a sample of 16 Compton-thick Seyfert 2 galaxies. The data were derived from Nandra et al. (1997), Bassani et al. (1999), and Ho & Peng (2001). We find $T_{\text{Sy1}} = 37.8 \pm 9.6$ and $T_{\text{Sy2}} = 3.7 \pm 1.1$. The average T for the FRIs of our sample is much larger than in Compton-thick Seyfert 2s, and actually consistent with Seyfert 1s. This result supports the idea that FRI radio galaxy lack a Compton-thick torus.

The detection of the compact X-ray core is not correlated with the presence of a dust lane. In fact, dust lanes are equally present in sources with ($\sim 55\%$) and without ($\sim 45\%$) a CCCX in our sample (de Koff et al. 2000; de Ruiter et al. 2002). In the cases where excess absorption is detected in the X-ray spectra and a dust lane is present, the column density from the X-rays and that due to the gas in the lane, $N_{H,V}$, are different. More precisely, comparing the values of $N_{H,V}$ from de Koff et al. (2000) and de Ruiter et al. (2002) to the values of N_H^z in Table 5, we find that the former is always about one order of magnitude smaller than the latter. This discrepancy was already reported previously for 3C 270 (e.g., Chiaberge et al. 2003) and is known to exist for other AGN (Maiolino, Marconi, & Oliva 2001). There are two possible interpretations: either the ratio of gas-to-dust in AGN is different than in the Galaxy (Maiolino, Marconi, & Oliva 2001), or the optical and X-ray extinction occur in distinct media (Weingartner & Murray 2002). The latter hypothesis was suggested by us for 3C 270 (Sambruna et al. 2003).

Thus, we conclude that FRIs lack a standard molecular torus, confirming the optical results. As discussed by CH99 and other authors, this implies that the lack of broad optical lines in these sources can not be due to obscuration, but to the absence of ionizing UV radiation, indicating inefficient accretion. Alternatively, the torus in FRIs may have a much smaller opening angle than in FRIIs, and/or lack significant cold gas. A survey of low-power radio galaxies in the far IR can also probe independently the presence of obscuration in the cores of these sources.

6.2. Origin of the X-rays in FRIs

The origin of the X-rays in radio galaxies in general, and in FRIs in particular, is still matter of considerable debate. The strong correlation between radio and X-ray core luminosities observed in low-luminosity (e.g., Fabbiano et al. 1984; Canosa et al. 1999) and high-luminosity (e.g., Worrall et al. 1994; Hardcastle et al. 1998) radio galaxies has often been used to argue in favor of a common origin from the unresolved base of the jet. However, such a correlation does not necessarily imply a common origin for

the radiation in the X-ray and radio regimes. Indeed, accretion processes and relativistic jets are widely believed to be correlated phenomena (e.g. Begelman et al. 1984) and, thus, a correlation between jet and accretion-related fluxes is naturally expected. In fact, Merloni, Heinz, & di Matteo (2003) have recently demonstrated that the correlation between X-ray and radio fluxes derives from a more general correlation (although with a substantial scatter) involving also the black hole masses (the so-called “fundamental plane”), where the radio is produced by the jet, whereas the X-rays are likely to be related to a radiatively inefficient accretion flow.

Previous studies of low-power AGN with *Chandra* demonstrate the importance of X-rays to make progress in this field (e.g., Di Matteo et al. 2001, 2003; Pellegrini et al. 2003; Terashima & Wilson 2003;). However, despite the high quality data provided by *Chandra*, the nature of the central engine in low-power AGN is still poorly known. Some authors (e.g., Fabbiano et al. 2003; Pellegrini et al. 2003) favor a jet-dominated scenario, where the entire spectral energy distribution (SED) can be explained in terms of non-thermal emission from the unresolved base of a jet. Others (e.g., Di Matteo et al. 2003; Ptak et al. 2004) favor a radiatively inefficient scenario where two solutions are possible: a) a high accretion rate \dot{M} (of the order of \dot{M}_{Bondi}) coupled with an extremely low radiative efficiency (basic ADAF scenario; see, e.g., Narayan 2002); or b) a moderate \dot{M} ($\ll \dot{M}_{\text{Bondi}}$) combined with a moderately low efficiency (more general RIAF scenario; see, e.g., Quataert 2003).

One of the reasons for this controversy is due to the poor discriminating power of the low-power AGN spectral data, which does not allow one to choose between the competing scenarios. In order to break this spectral degeneracy, additional model-independent constraints are required. Such information can be provided by the X-ray temporal and spectral variability properties, as well as by energetic considerations derived from the radio jet. This is the approach adopted by (Gliozzi, Sambruna, & Brandt 2003) to investigate the origin of the X-rays in the nuclear region of the nearby 3C 270. They found that the bulk of the X-ray emission originates from a radiatively inefficient accretion flow, with negligible jet contribution.

On the other hands, in this paper we find a correlation between the X-ray core flux of FRIs and the inclination angle of the jet. The trend is of decreasing X-ray luminosity with increasing orientation angle. This is expected if a fraction of the X-rays is beamed. It is thus possible that *both* the jet and a (radiatively inefficient; see below) accretion flow contribute to the production of the X-rays, with variable relative contributions. In support of this hypothesis, we note that in Figure 6b 3C 270 has an excess of X-rays over what expected from the jet, while M87 has a strong deficit.

More insightful results can be obtained from the spatial analysis, due to the unprecedented spatial resolution of *Chandra* that allows to disentangle the different components and to study the very inner region of the AGN. The first important results of this work is that a substantial fraction (9 out of 25) of FRI radio galaxies does not show a point-like component at high significance level (see Table 3).

The lack of CCCX among sources with an optical core may suggest a different origin between X-ray and optical emission. The latter was attributed to the base of the jet (CH99, Cao & Rawlings 2004). Further support to this hypothesis was lent by Kharb & Shastri (2004) who demonstrated the presence of a strong correlation between the optical point-like emission and the radio core dominance. On the other hands, the X-rays could be entirely produced in a very inefficient accretion flow.

Alternatively, the X-rays originate from the base of the jet, as suggested by the correlation we find between the inclination angle and the X-ray flux (Figure 6b). In this case, the lack of CCCX in sources with optical cores would place interesting constraints on the energy of the relativistic electrons and/or on the jet magnetic field.

6.3. Accretion in FRIs

The nature of the accretion process taking place onto the black hole in the nuclei of FRIs is another unanswered question. Previous studies of FRIs at X-ray (e.g., Sambruna et al. 1999; Di Matteo et al. 2001, 2003; Gliozzi, Sambruna, & Brandt 2003) favor an inefficient accretion process on the basis of the spectral energy distribution, energetic and temporal properties. However, for this specific sample of FRIs, Cao & Rawlings (2004) on the basis of *HST* observations and model-dependent theoretical considerations, have claimed that the accretion is efficient and takes place in form of a standard accretion disk (Shakura & Sunyaev 1973). A first model-independent way to test the nature of the accretion process at work in the FRI nuclei is based on the comparison between the Eddington and bolometric luminosities. In the following we assume the X-rays are due to the accretion process. The limits become even more severe if the X-rays are due in part or totally to the jet (see above).

The Eddington luminosity is readily obtained once the black hole mass is known. Luckily, the black hole masses of all the objects of our sample have been reported in literature (see Table 1). The bolometric luminosity has been estimated from the X-ray luminosity of the CCCX (i.e., the X-ray luminosity of the power-law component) assuming the canonical bolometric correction of 10 (e.g., Elvis et al. 1994). Incidentally, we note that the bolometric luminosities derived in this way are fully consistent with the ones derived from optical luminosities by Marchesini, Celotti, & Ferrarese (2004). The values of $L_{\text{bol}}/L_{\text{Edd}}$ for our sample, reported in Table 8, are quite low, ranging between 2×10^{-3} and 3×10^{-8} . These values are fully consistent with radiatively inefficient scenario and clearly inconsistent with a “standard” accretion disk, as in the case of Seyfert 1s, where the bolometric luminosity is a significant fraction (typically 10-30%) of the Eddington value.

An alternative model-independent method to assess the efficiency of the accretion process in FRIs is based on the direct estimate of the radiative efficiency η . This quantity can be readily obtained from the formula $L_{\text{bol}} = \eta \dot{M}_{\text{accr}} c^2$, where a rough estimate of the accretion rate is given by the Bondi accretion rate $\dot{M}_{\text{Bondi}} = 4\pi R_A^2 \rho_A c_s$, with accretion radius $R_A \sim GM/c_s^2$, c_s the sound speed, and ρ_A the density at the accretion radius.

The value of ρ_A can be derived either from a spatial method based on the deprojection of the surface bright-

ness profile, or from spectral method which makes use of the normalization of the thermal spectral component (see, e.g., Gliozzi et al. 2003, 2004 for a detailed description of either method). For *Chandra* observations with good quality brightness profiles, extending close to R_A the spatial method gives the most reliable results. On the other hand, for *XMM* observations the spectral method is preferable. The values of M_{Bondi} and η are reported in Table 8, and provide further support to the hypothesis that the accretion in FRIs is radiatively inefficient if X-rays come from accretion flow. To visualize the results we plot the histogram of the accretion rate in Eddington units in Figure 7. The Eddington accretion rate has been inferred assuming a canonical radiative efficiency of 0.1.

The only source with η marginally consistent with the standard accretion rates is 3C 28. However, in this case, as for all the sources in Table 8b, the values reported must be considered carefully. For this source there is not a CCCX detection and an upper limit of the X-ray luminosity has been used in the evaluation of L_{bol} and η .

7. SUMMARY

We have presented *Chandra* and *XMM* observations of FRIs from the 3CR and B2 catalogs, for which there are high-quality *HST* observations. The main findings of this paper can be summarized as follows:

- A thorough spatial analysis reveals that 13 out of the 25 objects in the sample exhibit a X-ray Central Compact Core (CCCX), for 3 of the sources the detection of a CCCX is uncertain, and for the remaining 9 sources no CCCX is found. All sources with a compact X-ray core also possess a compact core in the optical; however, some sources with an optical core lack a CCCX.

- All the FRIs are embedded in an extended component, which is fit by at least one β -model with parameters typical for a host galaxy and/or for an intracluster medium.

- The results from the spectral analysis are in good agreement with the spatial analysis. All the CCCX spectra

are well fit by power laws with photon indices $\Gamma \sim 1.1-2.6$, and at least one thermal component at softer energies. The remaining sources require only thermal components.

- Among the sources with CCCX, intrinsic absorption over the Galactic value is required in only 8 cases, with $N_H^z \sim 10^{20} - 10^{21} \text{ cm}^{-2}$. This result, combined with model-independent tests, supports the previous claim (e.g. Chiaberge, Capetti, & Celotti 1999) that low-power radio galaxies lack a standard molecular torus on pc-scales. As a consequence, the non-detection of CCCX cannot be attributed to obscuration effects, but rather to the intrinsic weakness of the AGN component.

- The origin of the X-rays (i.e., jet versus accretion) is still an open question. On the one hand, the non-detection of CCCX in objects with an optical CCC (interpreted as jet radiation) may indicate a different origin between X-ray and optical emission. On the other hand, the correlation between the *Chandra* X-ray luminosity and the inclination angle of the jet suggests that at least a fraction of the X-ray emission originates in the jet. However, the accretion flow can still play a role in the production of the X-rays in individual sources, as shown by our previous analysis of 3C 270.

- If the detected X-ray luminosities are considered as an upper limit on the isotropic component, stringent limits on the Eddington ratios $L_{\text{bol}}/L_{\text{Edd}}$ and on the accretion efficiency η can be derived, with $L_{\text{bol}}/L_{\text{Edd}} \sim 10^{-3} - 10^{-8}$ and $\eta \sim 10^{-2} - 10^{-6}$, suggesting radiatively inefficient accretion. The upper limits are even lower if part or all the X-rays are due to the jet.

We gratefully acknowledge the financial support provided by NASA grant G04-5115A (DD), and NASA LTSA grant NAG5-10708 (RMS, MG). RMS gratefully acknowledges support from an NSF CAREER award and from the Clare Boothe Luce Program of the Henry Luce Foundation.

REFERENCES

- Bassani, L., et al. 1999, *ApJS*, 121, 473
 Baum, S. A., et al. 1997, *ApJ*, 483, 178
 Begelman, M. C., Blandford, R. D., & Rees, M. J. 1984, *RvMP*, 56, 255
 Best, P. N., Bailer, D. M., Longair, M. S., & Riley, J. M. 1995, *MNRAS*, 275, 1171
 Bettoni, D., Falomo, R., Fasano, G., & Govoni, F. 2003, *A&A*, 399, 869
 Canosa, C. M., Worrall, D. M., Hardcastle, M. J., & Birkinshaw, M. 1999, *MNRAS*, 310, 30
 Cao, X., & Rawlings, S. 2004, *MNRAS*, 349, 1419
 Capetti, A., et al. 2002, *A&A*, 383, 104
 Cavaliere, A., & Fusco-Femiano, R. 1976, *A&A*, 49, 137
 Chiaberge, M., Capetti, A., & Celotti, A. 1999, *A&A*, 349, 77
 Chiaberge, M., Capetti, A., & Celotti, A. 2000, *A&A*, 355, 873
 Chiaberge, M., Gilli, R., Capetti, A., & Macchetto, F. D. 2003, *ApJ*, 597, 166
 Chiaberge, M., Gilli, R., Macchetto, F. D., Sparks, W. B., & Capetti, A. 2002, *MNRAS*, 334, 182
 Colla, G., et al. 1975, *A&AS*, 20, 1
 de Koff, S. et al. 2000, *ApJS*, 129, 33
 de Ruiter, H. R., Parma, P., Capetti, A., Fanti, R., Morganti, R. 2002, *ApJ*, 396, 857
 Dickey, J. M., & Lockman, F. J. 1990, *ARA&A*, 28, 215
 Di Matteo, T., Johnstone, R. M., Allen, S. W., & Fabian, A. C. 2001, *ApJ*, 550L, 19
 Di Matteo, T., Allen, S. W., Fabian, A. C., Wilson, A. S., & Young, A. J. 2003, *ApJ*, 582, 133
 Elvis, M., et al. 1994, *ApJS*, 95, 1
 Fabbiano, G., Trinchieri, G., Elvis, M., Miller, L., & Longair 1984, *ApJ*, 277, 115
 Fabbiano, G., et al. 2003, *ApJ*, 588, 175
 Fanti, R., Gioia, I., Lari, C., & Ulrich, M. H. 1978, *A&AS*, 34, 341
 Feretti, L., & Giovannini, G. 1987, *A&A*, 182, 15
 Ge, J. P., & Owen, F. N. 1993, *AJ*, 105, 778
 Ghisellini, G., & Celotti, A. 2001, *A&A*, 379, L1
 Ghizzardi, S. 2001, *XMM-Newton Calibration Document* EPIC-MCT-TN-011 (XMM-SOC-CAL-TN-0022), available at http://xmm.vilspa.esa.es/external/xmm_sw_cal/calib/documentation.shtml#EPIC
 Giovannini, G., Cotton, W. D., Feretti, L., Lara, L., & Venturi, T. 2001, *ApJ*, 552, 508
 Gliozzi, M., Sambruna, R. M., & Brandt, W. N. 2003, *A&A*, 408, 949
 Gliozzi, M., Sambruna, R. M., Brandt, W. N., Mushotzky, R., & Eracleous, M. 2004, *A&A*, 413, 139
 Hardcastle, M. J., Worrall, D. M., & Birkinshaw, M. 1998, *MNRAS*, 296, 1098
 Hardcastle, M. J., & Worrall, D. M. 2000, *MNRAS*, 314, 359
 Hardcastle, M. J., Birkinshaw, M., & Worrall, D. M. 2001, *MNRAS*, 326, 1499
 Hardcastle, M. J., Worrall, D. M., Birkinshaw, M., Laing, R. A., & Bridle, A. H. 2002, *MNRAS*, 334, 182
 Harris, D. E. 2003, *NewAR*, 47, 617
 Ho, L. C., & Peng, C. Y. 2001, *ApJ*, 555, 650
 Kharb, P., & Shastri, P. 2004, *astro-ph/0401042*
 Laing, R. A., Riley, J. M., & Longair, M. S. 1983, *MNRAS*, 204, 151

- Laing, R. A., Parma, P., de Ruiter, H. R., & Fanti R. 1999, MNRAS, 306, 513
- Lavalley, M., Isobe, T., & Feigelson, E. D. 1992, BAAS, 24, 839
- Maiolino, R., Marconi, A., & Oliva, E. A&A, 365, 37
- Marchesini, D., Celotti, A., & Ferrarese, L. 2004, MNRAS, 351, 733
- Marshall, H. L., et al. 2002, ApJ, 564, 683
- Matt, G., et al. 2000, MNRAS, 318, 173
- Merloni, A., Heinz, S., & Di Matteo, T. 2003, MNRAS, 345, 1057
- Nandra, K., George, I. M., Mushotzky, R. F., Turner, T. J., & Yaqoob, T. 1997, ApJ, 477, 602
- Narayan, R. 2002, in Lighthouses of the Universe: The Most Luminous Celestial Objects and Their Use for Cosmology. Proceedings of the MPA/ESO/, 405 (astro-ph/0201260)
- Pedlar, A., et al. 1990, MNRAS, 246, 477
- Pellegrini, S., et al. 2003, ApJ, 585, 677
- Piner, B. G., Jones, D. L., & Wehrle, A. E. 2001, AJ, 122, 2954
- Ptak, A., Terashima, Y., Ho, L. C., & Quataert, E. 2004, ApJ, 606, 173
- Quataert, E. 2003, Astron. Nachr., 324, 435
- Quillen, A. C., Almog, J., Yukita, M. 2003, AJ, 126, 2677
- Rawlings, S., Saunders, R., Eales, S. A., & Mackay, C. D. 1989, MNRAS, 240, 701
- Reynolds, C.S., Di Matteo, T., Fabian, A.C., Hwang, U., & Canizares, C.R. 1996, MNRAS, 283, 111
- Sambruna, R.M., Eracleous, M., & Mushotzky, R.F. 1999, ApJ, 526, 60
- Sambruna, R.M., Gliozzi, M., Eracleous, M., Brandt, W. N., & Mushotzky, R.F. 2003, ApJ, 586L, 37
- Saxton, C. J., Bicknell, G. V., & Sutherland, R. S. 2002, ApJ, 579, 176
- Shakura, N.I., & Sunyaev, R.A. 1973, A&A, 24, 337
- Sparks, W. B., et al. 1995, ApJ, 450L, 55
- Spinrad, H., Djorgovski, S., Marr, J., & Aguilar, L. 1985, PASP, 97, 932
- Terashima, Y. & Wilson, A. S. 2003, ApJ, 583, 145
- Turner, T. J., George, I. M., Mushotzky, R. F., & Nandra, K. 1997, ApJ, 475, 118
- Venturi, T., Morganti, R., Tzioumis, T., & Reynolds, J. 2000, A&A, 363, 84
- Weingartner, J. C., & Murray, N. 2002, ApJ, 580, 88
- Wilson, A. S. & Yang, Y. 2002, ApJ, 568, 133
- Woo, J.-H., & Urry, C. M. 2003, ApJ, 579, 530
- Worrall, D. M., & Birkinshaw, M. 1994, ApJ, 427, 134
- Worrall, D. M., & Birkinshaw, M. 2000, ApJ, 530, 719
- Worrall, D. M., Birkinshaw, M., & Hardcastle, M. J. 2001, MNRAS, 326, L7
- Worrall, D. M., Birkinshaw, M., & Hardcastle, M. J. 2003, MNRAS, 343, 73
- Zirbel, E. L., & Baum, S. A. 1995, ApJ, 448, 521

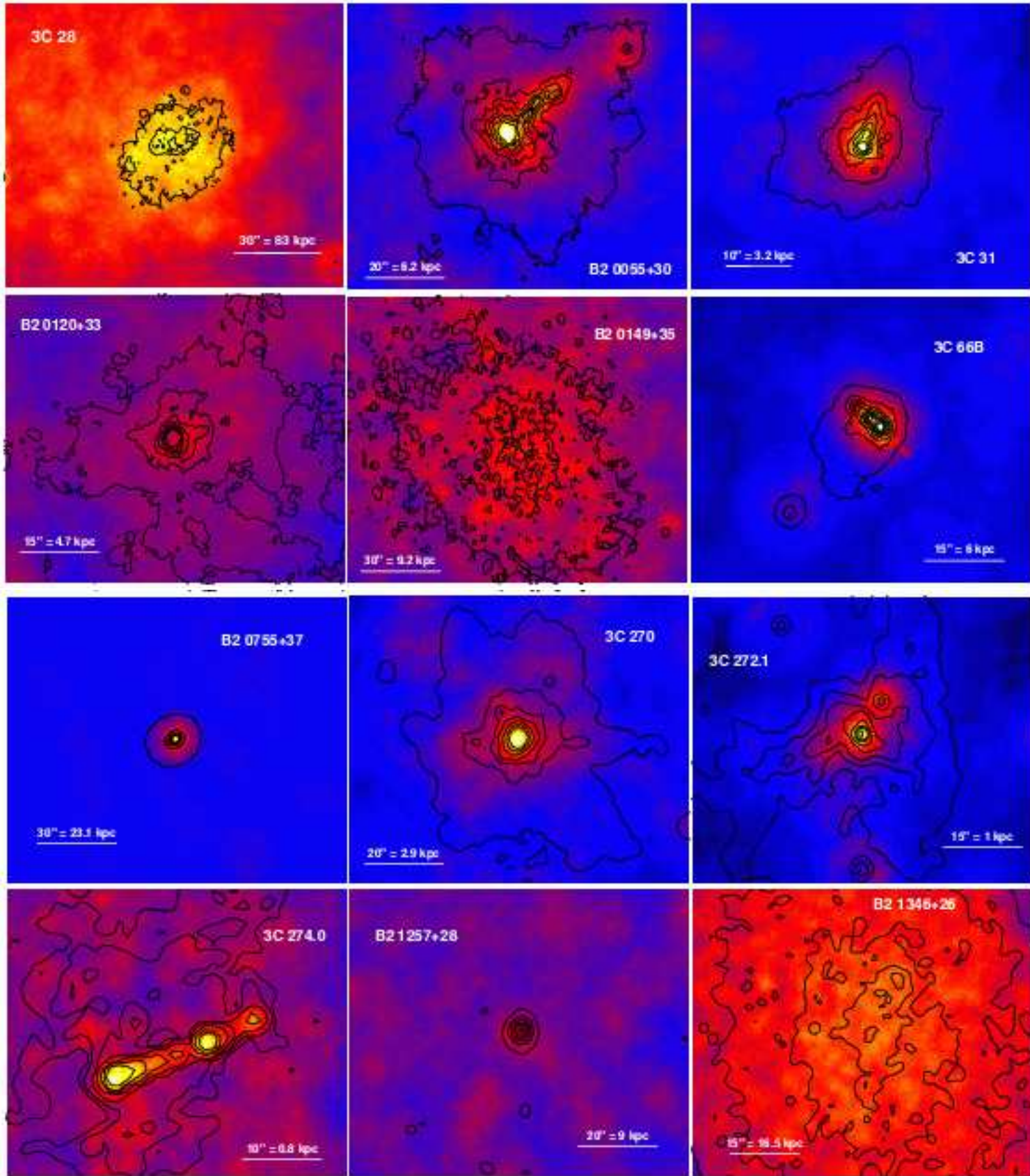


FIG. 1.— Hard X-ray (2–8 keV) images of the FRI radio galaxies of our sample, with the soft X-ray (0.3–2 keV) contours overlaid. All images were obtained with the ACIS cameras on *Chandra*. The soft and hard X-ray images were smoothed using the sub-package `fadapt` of `FTOOLS` with a circular top hat filter of adaptive size in order to achieve a minimal number of 10 counts under the filter. A hard X-ray point source, embedded in diffuse soft X-ray emission, is generally present (see Table 3).

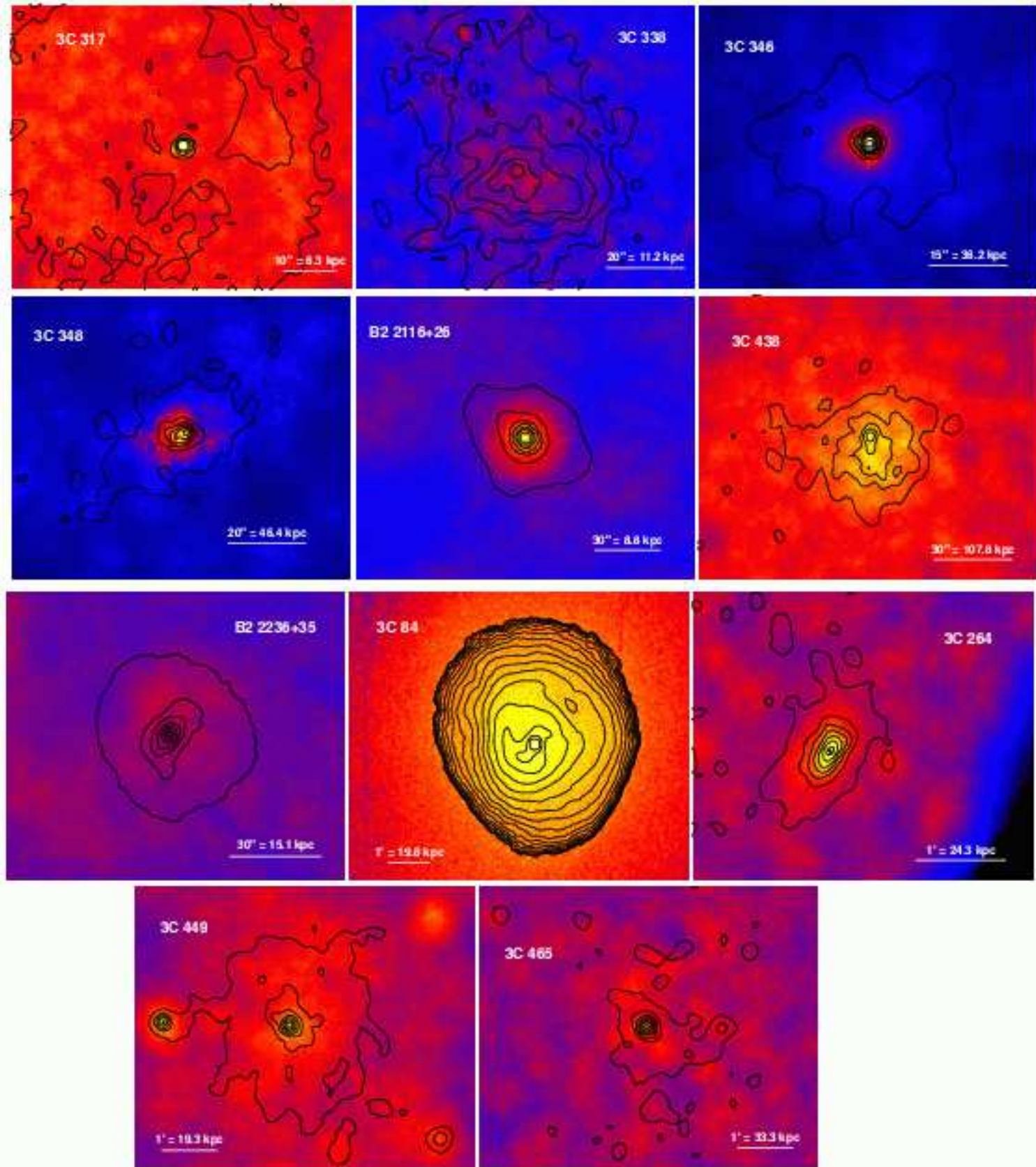


FIG. 2.— Same as for Figure 1, except that the X-ray images for 3C 84, 3C 264, 3C 449, and 3C 465 are from *XMM* EPIC MOS1.

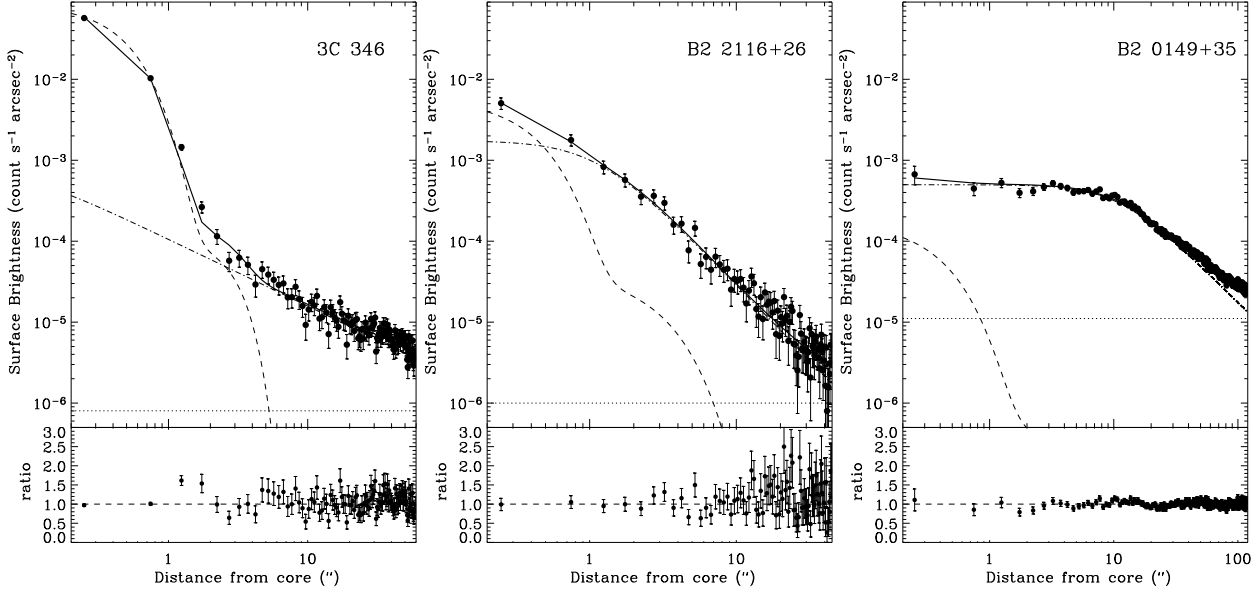


FIG. 3.— Examples of radial profiles for three sources observed with ACIS. In the top panels, the dashed line is the instrumental PSF, and the dot-dashed line the β -model describing the diffuse emission. The continuous thick line is the total model, while the thin dotted horizontal line is the background. The residuals of the best-fit model are shown in the bottom panels. The PSF is detected with high ($> 99.9\%$) significance in 3C 346, moderate ($\sim 96\%$) significance in B2 2116+26, while it is not requested in the case of B2 0149+35.

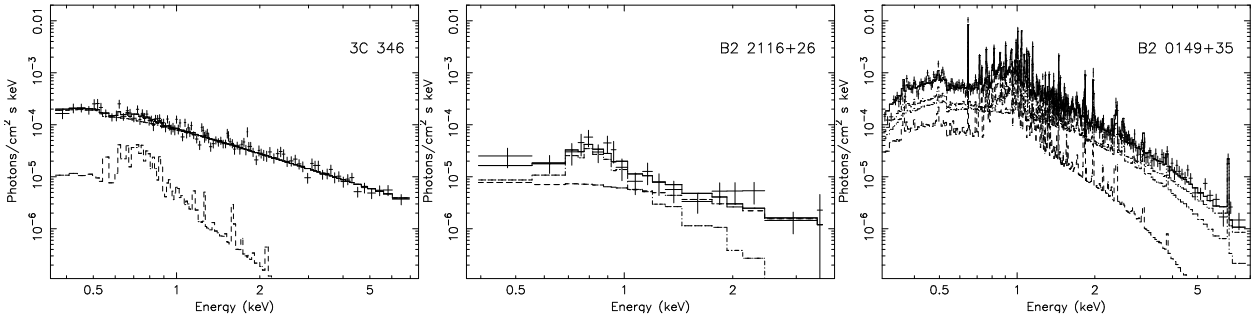


FIG. 4.— X-ray spectra for the three sources presented in Figure 3. In agreement with the spatial analysis, a power-law component is required for 3C 346, partially required for B2 2116+26, and no required for B2 0149+35.

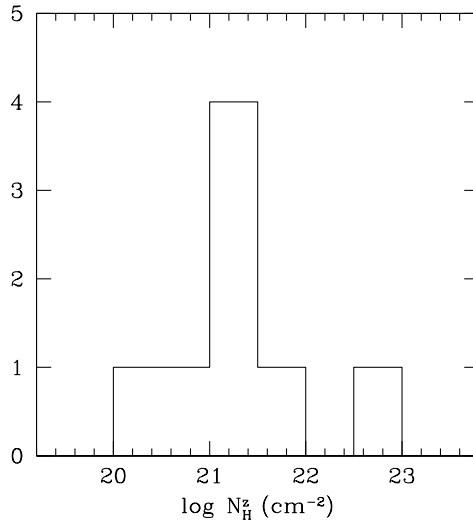


FIG. 5.— Histogram of the intrinsic absorption obtained from the spectra of sources with detected CCCX.

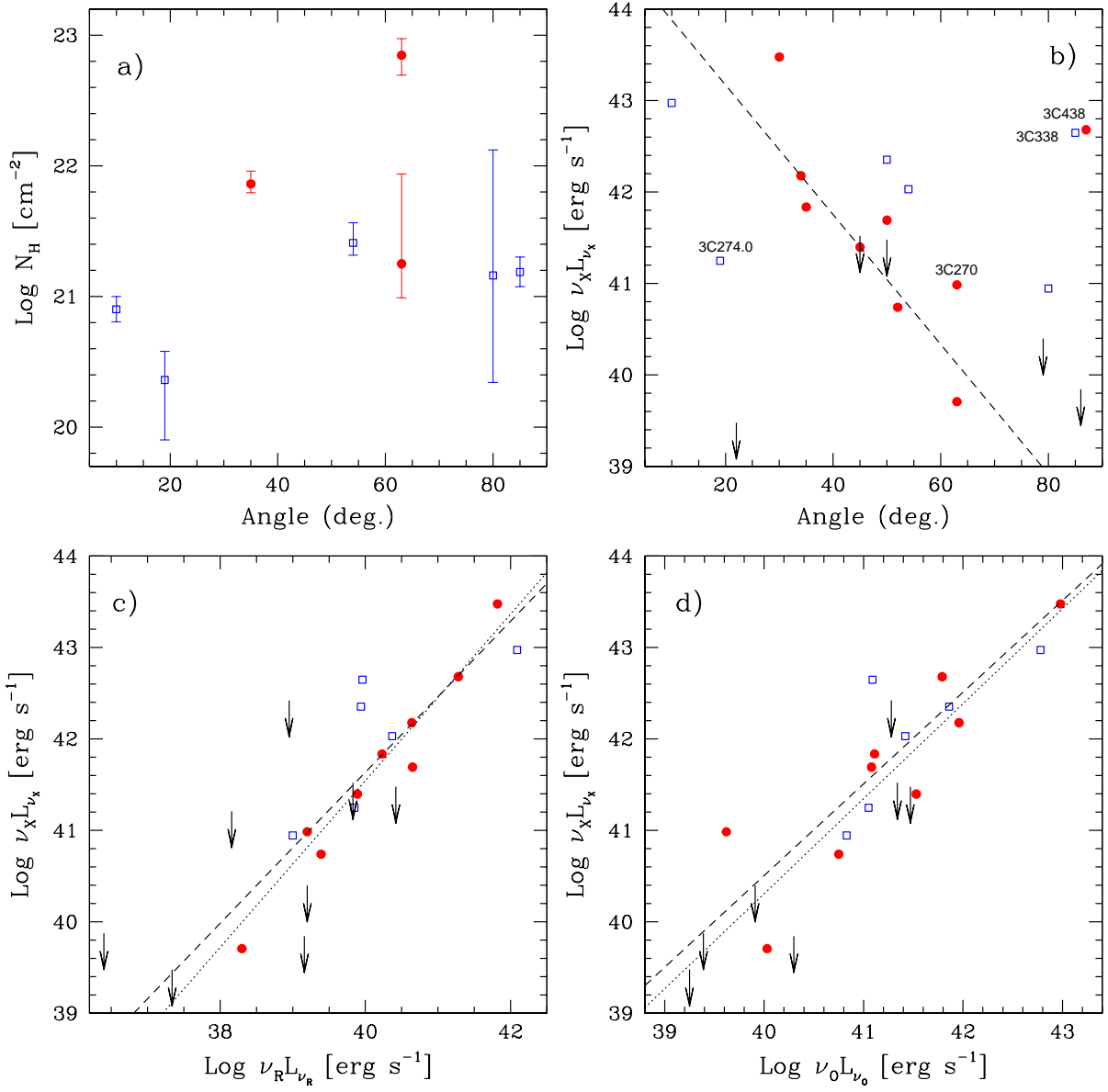


FIG. 6.— Top panels: Plots of the inclination angle of the radio jet versus the intrinsic column density from the X-ray spectral fits (a) and versus the core X-ray luminosity in 0.3–8 keV (b). Bottom panels: Plots of the core X-ray luminosity versus the radio luminosity (c) and the optical luminosity (d). Filled circles are parameters from the *Chandra* data, open squares from the *XMM* data. The dashed line is from a linear regression analysis of the firm detections, while the dotted line is from an analysis including upper limits.

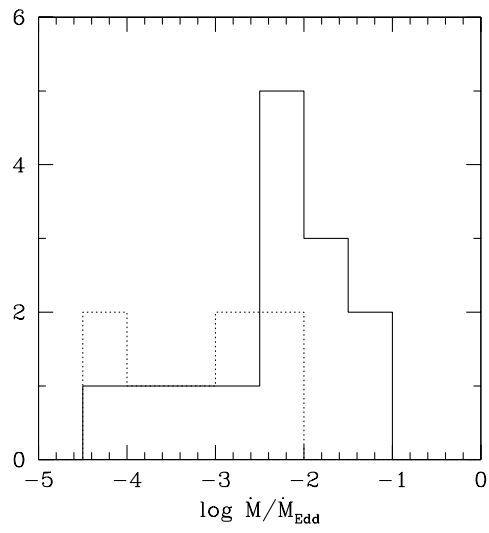


FIG. 7.— Histogram of the accretion rate in Eddington units. The solid line refers to sources with confirmed CCCX; the dotted line refers to sources with upper limit to CCCX. The Eddington accretion rate has been inferred assuming a canonical radiative efficiency of 0.1.

TABLE 1
THE SAMPLE

Source (1)	Other name (2)	z (3)	$N_{\text{H,Gal}}$ (4)	Angle (5)	Ref. (6)	$\text{Log}M_{\text{BH}}$ (7)	$\text{Log}(\nu_r L_{\nu_r})$ (8)	$\text{Log}(\nu_o L_{\nu_o})$ (9)
3C 28		0.1953	5.40			8.67	38.95	41.28
B2 0055+30	NGC 315	0.0165	5.86	35 ^a	Gi01	9.18	40.23	41.11
3C 31	NGC 383	0.0170	5.36	52	Ha02	7.89	39.39	40.75
B2 0120+33	NGC 507	0.0165	5.25			8.94	36.40	39.39
B2 0149+35	NGC 708	0.0162	5.29			8.46 ^b	38.16	Dusty
3C 66B		0.0213	9.15	45	Ha01	8.84	39.89	41.53
3C 78	NGC 1218	0.0287	10.70	30	Sp95	8.98	40.87	42.43
3C 84	NGC 1275	0.0176	15.70	10	Pe90	9.28	42.09	42.78
B2 0755+37	NGC 2484	0.0428	5.07	34	La99	8.93	40.64	41.96
3C 264	NGC 3862	0.0217	2.19	50	Ba97	8.85	39.94	41.86
3C 270	NGC 4261	0.0075	1.52	63	Pi01	8.57	39.20	39.62
3C 272.1	M 84	0.0035	2.63	63 ^a	Gi01	8.35	38.30	40.03
3C 274.0	M 87	0.0044	2.59	19	Gi01	8.26	39.85	41.05
B2 1256+28	NGC 4869	0.0229	0.89			8.12 ^b	37.69	Dusty
B2 1257+28	NGC 4874	0.0241	0.89	22 ^a	Fe87	8.63	37.34	39.25
B2 1346+26	4C26.42	0.0633	1.18	45	Ge93	9.02	39.83	41.34
3C 317	UGC 9799	0.0345	2.90	50 ^a	Ve00	8.80	40.65	41.08
3C 338	NGC 6166	0.0304	0.84	85	Gi01	9.23	39.96	41.09
3C 346		0.1620	5.67	30	Gi01	8.89	41.82	42.98
3C 348	Her A	0.1540	6.28	50 ^a	Sa02	8.84	40.42	41.47
B2 2116+26	NGC 7052	0.0156	12.90	79	La99	8.60	39.20	39.91
3C 438		0.2900	19.70	87 ^a	Be95	8.80	41.28	41.79
3C 449	UGC 12064	0.0171	12.00	80	Ha98	8.42 ^c	39.00	40.83
B2 2236+35	UGC 12127	0.0276	10.00	86	La99	8.55	39.16	40.30
3C 465	NGC 7720	0.0302	4.84	54	Gi01	9.32	40.37	41.42

Column Explanation: 1=Source name; 2=Alternative name; 3=Redshift; 4=Galactic column density in 10^{20} cm^{-2} , from Dickey & Lockman (1990); 5=Inclination angle in degrees of the jet axis with respect the line of sight (^a=Average value); 6=Reference for column 5. Ba97=Baum 1997; Be95=Best 1995; Fe87=Feretti 1987; Ge93=Ge 1993; Gi01=Giovannini 2001; Ha98=Hardcastle 1998; Ha01=Hardcastle 2001; Ha02=Hardcastle 2002; La99=Laing 1999; Pe90=Pedlar 1990; Pi01=Piner 2001; Sa02=Saxton 2002; Sp95=Sparks 1995; Ve00=Venturi 2000. 7=Black hole mass in solar masses (Marchesini et al. 2004; ^b=Woo & Urry 2003; ^c=Bettoni et al. 2003); 8=Core radio luminosity at 5 GHz, in erg s^{-1} , from Colla et al. (1975); 9=Core optical luminosity, in erg s^{-1} , from CH99, CA02.

TABLE 2
OBSERVATION LOG

Source (1)	Satellite (2)	Date (3)	Net Exp. (4)	Count Rate (5)
3C 28	<i>Chandra</i>	2002-10-07	48.73	0.023±0.001
B2 0055+30	<i>Chandra</i>	2003-02-22	51.28	0.108±0.001
3C 31	<i>Chandra</i>	2000-11-06	42.52	0.039±0.001
B2 0120+33	<i>Chandra</i>	2000-10-11	18.26	0.035±0.001
	<i>XMM</i>	2001-01-15	26.56	0.082±0.002
B2 0149+35	<i>Chandra</i>	2001-08-03	28.74	0.037±0.001
	<i>XMM</i>	2001-01-16	17.42	1.020±0.008
3C 66B	<i>Chandra</i>	2000-11-20	28.36	0.043±0.001
3C 78	<i>Chandra</i>	2001-12-16	5.23	0.224±0.007
3C 84	<i>XMM</i>	2001-01-30	24.71	11.648±0.022
B2 0755+37	<i>Chandra</i>	2000-04-03	5.61	0.098±0.004
3C 264	<i>XMM</i>	2001-05-26	24.12	0.228±0.003
3C 270	<i>Chandra</i>	2000-05-06	32.51	0.126±0.002
3C 272.1	<i>Chandra</i>	2000-05-19	28.19	0.075±0.002
3C 274.0	<i>Chandra</i>	2000-07-30	12.69	0.521±0.006
	<i>XMM</i>	2000-06-19	25.38	1.913±0.010
B2 1256+28	<i>XMM</i>	2001-12-04	22.61	<0.617 ^a
B2 1257+28	<i>Chandra</i>	1999-11-04	9.53	0.020±0.002
B2 1346+26	<i>Chandra</i>	2004-01-14	14.30	0.113±0.003
3C 317	<i>Chandra</i>	2000-09-03	36.20	0.077±0.001
3C 338	<i>Chandra</i>	1999-12-11	16.94	0.118±0.003
	<i>XMM</i>	2002-08-15	5.77	2.999±0.023
3C 346	<i>Chandra</i>	2002-08-03	39.75	0.079±0.001
3C 348	<i>Chandra</i>	2001-07-25	14.58	0.047±0.002
B2 2116+26	<i>Chandra</i>	2002-09-21	9.63	0.028±0.002
3C 438	<i>Chandra</i>	2002-12-27	37.06	0.016±0.001
3C 449	<i>XMM</i>	2001-12-09	16.71	0.087±0.002
B2 2236+35	<i>Chandra</i>	2001-05-13	9.39	0.021±0.001
3C 465	<i>XMM</i>	2002-06-22	4.48	0.148±0.006

^a 3σ upper limit.

Columns explanation: 1=Source name; 2=Instrument; 3=Observation date (yyyy-mm-dd); 4=Live time in ksec after data screening. For *XMM* observations, the exposures refer to data taken with the EPIC pn camera; 5=Total source count rate in the 0.3-8 keV energy range. The extraction radius is 5'' for *Chandra* and 30'' for *XMM*, except for B2 0120+33 and 3C 264 (12'') and for 3C274.0 (9'').

TABLE 3
RESULTS OF THE X-RAY SPATIAL ANALYSIS

Source	CCC		Core Sig.	Sat.	Count Rate
(1)	opt.	X	(4)	(5)	(6)
	(2)	(3)			
3C 28	Up	N	92.9%	C	<0.001
B2 0055+30	Up	Y	>99.9%	C	0.035±0.001
3C 31	Y	Y	>99.9%	C	0.003±0.001
B2 0120+33	Up	N	12.4%	C	<0.001
B2 0149+35	D	N	38.7%	C	<0.001
3C 66B	Y	Y	>99.9%	C	0.006±0.001
3C 78	Y	U	...	C	0.053±0.003
3C 84	Y	Y	>99.9%	X	2.815±0.011
B2 0755+37	Y	Y	>99.9%	C	0.009±0.001
3C 264	Y	U	...	X	0.020±0.001
3C 270	Y	Y	99.9%	C	0.016±0.001
3C 272.1	Y	U	...	C	0.005±0.001
3C 274.0	Y	Y	>99.9%	C	0.052±0.002
B2 1256+28	D	N	...	X	<0.160 ^a
B2 1257+28	Up	N	30.2%	C	<0.001
B2 1346+26	Y	N	22.3%	C	0.002±0.001
3C 317	Y	Y	>99.9%	C	0.006±0.001
3C 338	Y	Y	99.9%	C	0.002±0.001
3C 346	Y	Y	>99.9%	C	0.017±0.001
3C 348	Y	N	21.4%	C	<0.001
B2 2116+26	Y	N	95.6%	C	0.002±0.001
3C 438	Up	Y	>99.9%	C	<0.001
3C 449	Y	Y	>99.9%	X	0.012±0.001
B2 2236+35	Y	N	15.4%	C	<0.001
3C 465	Y	Y	>99.9%	X	0.023±0.002

^a 3σ upper limit.

Columns Explanation: 1=Source name; 2=Detection of the optical Central Compact Core: Y=Yes, D=Dusty galaxy; Up=Upper limit (CH99, CA02); 3=Detection of the X-ray Central Compact Core: Y=Yes, N=No, U=Uncertain; 4=Significance of the PSF, from the F-test; 5=C: *Chandra*; X: *XMM*; 6=X-ray count rate of the core in the energy range 2–10 keV from an extraction radius of 1.5".

TABLE 4
RESULTS OF FITS OF RADIAL PROFILES

Source (1)	Core Radius (2)	β (3)	Norm. (4)
3C 28	6.24±0.58	0.42±0.04	3.2±0.1
B2 0055+30	1.98±0.20	0.54±0.03	23.8±3.2
3C 31	3.46±0.39	0.68±0.10	7.0±0.8
B2 0120+33 ^a	0.59±0.09	0.46±0.04	52.3±7.5
B2 0149+35	11.16±0.54	0.42±0.02	5.0±0.1
3C 66B	0.49±1.02	0.49±0.07	45.4±17.0
3C 84	104.09±0.76	0.64±0.01	11.6±0.1
B2 0755+37	0.59±0.59	0.60±0.16	107.5±107.5
3C 270	0.98±0.07	0.52±0.01	126.7±14.5
3C 274.0	0.22±0.20	0.24±0.01	104.6±43.2
B2 1257+28	1.48±0.15	0.67±0.01	16.7±2.9
B2 1346+26	3.32±0.54	0.25±0.01	16.1±0.9
3C 317	38.61±0.22	0.67±0.01	5.8±0.1
3C 338	12.91±0.36	0.34±0.01	11.5±0.2
3C 346	0.10±0.10	0.30±0.06	7.3±6.6
3C 348 ^a	4.05±0.70	0.75±0.30	11.5±1.1
B2 2116+26	1.11±0.28	0.48±0.03	17.5±6.2
3C 438 ^a	13.81±2.89	0.87±0.61	1.9±0.1
3C 449	106.20±54.62	0.71±0.14	<0.1
B2 2236+35	0.74±0.15	0.48±0.04	26.7±6.4
3C 465	194.50±43.44	0.60±0.34	<0.1

^a An additional β -model is necessary.

Columns Explanation: 1=Source name; 2=Core radius in arcseconds; 3= β parameter; 4=Normalization of the β -model in units of 10^{-4} counts s^{-1} arcsec $^{-2}$. Uncertain detections (3C 78, 3C 264, and 3C 272.1) are not considered

TABLE 5
CORE X-RAY SPECTRAL ANALYSIS

		Thermal Model				Power-law		$\chi^2_{\text{red}}/\text{d.o.f.}$ (9)
Source (1)	(2)	kT ₁ (3)	Z ₁ (4)	kT ₂ (5)	Z ₂ (6)	N^z_H (7)	Γ (8)	
a) Confirmed CCCX								
B2 0055+30	C	$0.51^{+0.05}_{-0.05}$	1.0	$72.7^{+18.4}_{-10.5}$	$1.56^{+0.17}_{-0.09}$	0.97/153
3C 31	C	$0.69^{+0.06}_{-0.05}$	0.2	$1.22^{+0.27}_{-0.19}$	1.03/33
3C 66B	C	$0.36^{+0.16}_{-0.07}$	1.0	$2.17^{+0.14}_{-0.15}$	0.91/45
3C 84 ^a	X	$2.38^{+0.37}_{-0.40}$	1.0	$0.82^{+0.17}_{-0.47}$	0.2	$8.0^{+2.}_{-1.6}$	$1.86^{+0.05}_{-0.05}$	1.29/460
B2 0755+37	C	$0.26^{+0.14}_{-0.18}$	0.2	$2.18^{+0.28}_{-0.19}$	0.67/15
3C 270	C	$0.60^{+0.03}_{-0.03}$	1.0	$702.6^{+238.7}_{-207.2}$	$1.09^{+0.44}_{-0.23}$	1.04/60
3C 274.0 ^b	X	$0.10^{+0.94}_{-0.02}$	0.2	$1.66^{+0.05}_{-0.05}$	1.0	$2.3^{+1.5}_{-1.5}$	$2.40^{+0.08}_{-0.06}$	1.31/575
3C 317	C	$0.18^{+0.09}_{-0.04}$	1.0	$0.80^{+0.68}_{-0.21}$	1.0	...	$1.81^{+0.13}_{-0.10}$	0.98/52
3C 338	X	$2.23^{+0.18}_{-0.16}$	1.0	$0.15^{+0.06}_{-0.04}$	1.0	$15.4^{+4.7}_{-3.5}$	$2.15^{+0.16}_{-0.19}$	0.94/569
3C 346	C	$0.64^{+0.40}_{-0.38}$	0.2	$1.69^{+0.09}_{-0.09}$	1.06/101
3C 438	C	$1.54^{+0.30}_{-0.26}$	231.1/321 ^c
3C 449	X	$0.58^{+0.15}_{-0.27}$	0.2	$1.26^{+0.26}_{-0.20}$	1.0	$14.5^{+117.9}_{-12.3}$	$2.13^{+0.65}_{-0.55}$	0.95/58
3C 465	X	$0.97^{+0.08}_{-0.08}$	1.0	...	1.0	$25.7^{+10.9}_{-5.}$	$2.59^{+0.37}_{-0.20}$	0.86/41
b) Candidate CCCX								
3C 264	X	$0.33^{+0.08}_{-0.06}$	0.2	$2.48^{+0.04}_{-0.04}$	0.92/290
3C 272.1	C	$0.61^{+0.14}_{-0.19}$	0.8	$17.8^{+69.}_{-8.}$	$2.06^{+0.31}_{-0.29}$	0.61/28

^a Additional thermal component necessary: $kT_3=0.17\pm 0.02$, $Z_3 \cong 0.6$

^b Additional thermal component necessary: $kT_3=0.81\pm 0.02$, $Z_3 \cong 0.5$

^c Values of C-statistics and PHA bins.

Columns Explanation: 1=Source name; 2=Satellite data used for the spectral analysis (C=*Chandra*, X=*XMM*); 3-6=Temperature kT in keV and abundance Z/Z_\odot ; 7-8=Absorption column density at the source's redshift, in 10^{20} cm^{-2} ; Photon index Γ of the power-law component; 9=Reduced χ^2 of the fit and degrees of freedom.

TABLE 6
SOURCES X-RAY FLUXES AND LUMINOSITIES

Source (1)	Total		Power-law	
	Flux (2)	Lum. (3)	Flux (4)	Lum. (5)
a) Confirmed CCCX				
B2 0055+30	0.88	0.72	0.84	0.69
3C 31	0.14	0.08	0.10	0.05
3C 66B	0.23	0.27	0.21	0.25
3C 84	14.10	12.40	11.10	9.40
B2 0755+37	0.39	1.73	0.35	1.51
3C 264	2.24	2.35	2.12	2.26
3C 270	0.59	0.11	0.49	0.10
3C 272.1	0.16	0.01	0.14	0.01
3C 274.0	7.28	0.32	3.76	0.18
3C 317	0.22	0.60	0.20	0.49
3C 338	4.45	9.57	1.66	4.44
3C 346	0.48	31.05	0.47	30.24
3C 438	0.04	4.78	0.04	4.78
3C 449	0.17	0.16	0.09	0.09
3C 465	0.32	1.18	0.25	1.07
b) Upper Limits to CCCX (3σ)				
3C 28	0.18	16.94	<0.03	<2.64
B2 0120+33	0.25	0.16	<0.01	<0.01
B2 0149+35	2.36	1.59	<0.23	<0.16
B2 1257+28	0.06	0.07	<0.01	<0.01
B2 1346+26	0.68	6.60	<0.03	<0.33
3C 348	0.09	5.91	<0.01	<0.30
B2 2116+26	0.07	0.04	<0.05	<0.03
B2 2236+35	0.03	0.14	<0.01	<0.01

Columns Explanation: 1=Source name; 2-3=Observed total flux and intrinsic luminosity in 0.3–8 keV of the source; 4-5=Observed flux and intrinsic luminosity in 0.3–8 keV for AGN. The fluxes are expressed in 10^{-12} erg cm^{-2} s^{-1} and the luminosities in 10^{42} erg s^{-1} .

TABLE 7
CORRELATION PROBABILITIES AND PARAMETERS

	P_r (1)	$ r $ (2)	a (3)	b
a) Detections only				
Angle / $\text{Log } N_H$	33.9	0.36	20.930	0.005
$\text{Log } \nu_X L_{\nu_X} / \text{Log } N_H$	58.2	0.21	22.984	-0.044
Angle / $\text{Log } \nu_X L_{\nu_X}$	42.4	0.22	42.937	-0.025
	0.5	0.87	44.590	-0.071
$\text{Log } \nu_R L_{\nu_R} / \text{Log } \nu_X L_{\nu_X}$	6.8E-4	0.89	8.596	0.826
$\text{Log } \nu_O L_{\nu_O} / \text{Log } \nu_X L_{\nu_X}$	6.2E-3	0.85	0.427	1.002
a) Detections + Upper limits				
Angle / $\text{Log } \nu_X L_{\nu_X}$	13.5	...	42.519	-0.018
$\text{Log } \nu_R L_{\nu_R} / \text{Log } \nu_X L_{\nu_X}$	0.0	...	5.101	0.911
$\text{Log } \nu_O L_{\nu_O} / \text{Log } \nu_X L_{\nu_X}$	0.0	...	-1.253	1.039

Columns Explanation: 1=Probability (in %) that the distribution is generated by a random population. A small probability indicates a significant correlation; 2=Linear coefficient from a linear regression analysis; 3-4=Coefficients of the linear regression parameters a and b (where $y=a+bx$).

TABLE 8
ACCRETION PROPERTIES

Source (1)	\dot{M}_{Bondi} (2)	$L_{\text{bol}}/L_{\text{Edd}}$ (3)	η (4)
a) Confirmed CCCX			
B2 0055+30	$4.6 \cdot 10^{-1}$	$2.6 \cdot 10^{-5}$	$1.9 \cdot 10^{-4}$
3C 31	$3.5 \cdot 10^{-4}$	$5.3 \cdot 10^{-5}$	$2.6 \cdot 10^{-2}$
3C 66B	$3.9 \cdot 10^{-1}$	$1.2 \cdot 10^{-5}$	$4.5 \cdot 10^{-5}$
3C 84 ^a	$3.0 \cdot 10^{-1}$	$2.2 \cdot 10^{-4}$	$3.1 \cdot 10^{-3}$
B2 0755+37 ^a	$6.0 \cdot 10^{-1}$	$5.9 \cdot 10^{-5}$	$1.9 \cdot 10^{-4}$
3C 264 ^a	$5.1 \cdot 10^{-2}$	$6.7 \cdot 10^{-5}$	$2.1 \cdot 10^{-3}$
3C 270	$9.5 \cdot 10^{-2}$	$2.1 \cdot 10^{-5}$	$1.8 \cdot 10^{-4}$
3C 272.1 ^a	$3.1 \cdot 10^{-1}$	$8.3 \cdot 10^{-7}$	$1.3 \cdot 10^{-6}$
3C 274.0	$1.7 \cdot 10^{-2}$	$2.2 \cdot 10^{-5}$	$5.3 \cdot 10^{-4}$
3C 317	$6.1 \cdot 10^{-2}$	$3.6 \cdot 10^{-5}$	$8.3 \cdot 10^{-4}$
3C 338	$8.7 \cdot 10^{-3}$	$8.7 \cdot 10^{-5}$	$3.8 \cdot 10^{-2}$
3C 346	$5.3 \cdot 10^{-2}$	$2.0 \cdot 10^{-3}$	$6.5 \cdot 10^{-2}$
3C 449 ^a	$1.0 \cdot 10^{-4}$	$5.7 \cdot 10^{-5}$	$6.6 \cdot 10^{-2}$
3C 465 ^a	$2.5 \cdot 10^{-2}$	$9.4 \cdot 10^{-6}$	$1.8 \cdot 10^{-2}$
b) Undetected CCCX			
3C 28	$5.8 \cdot 10^{-4}$	$1.2 \cdot 10^{-4}$	$2.2 \cdot 10^{-1}$
B2 0120+33	$1.8 \cdot 10^{-1}$	$5.0 \cdot 10^{-7}$	$5.4 \cdot 10^{-6}$
B2 0149+35	$6.2 \cdot 10^{-4}$	$9.0 \cdot 10^{-6}$	$9.3 \cdot 10^{-3}$
B2 1257+28	$1.5 \cdot 10^{-2}$	$3.2 \cdot 10^{-8}$	$2.0 \cdot 10^{-6}$
B2 1346+26	$9.2 \cdot 10^{-3}$	$1.4 \cdot 10^{-5}$	$3.6 \cdot 10^{-3}$
3C 348	$3.2 \cdot 10^{-3}$	$2.4 \cdot 10^{-5}$	$1.1 \cdot 10^{-2}$
B2 2116+26	$3.2 \cdot 10^{-2}$	$3.7 \cdot 10^{-6}$	$1.0 \cdot 10^{-4}$
B2 2236+35	$1.9 \cdot 10^{-2}$	$6.6 \cdot 10^{-7}$	$2.7 \cdot 10^{-5}$

^a Calculated assuming parameters from the spectral analysis (see text).

Columns Explanation: 1=Source name; 2=Bondi accretion rate (M_{\odot}/yr); 3=Ratio of the bolometric luminosity to the Eddington luminosity; 4=Radiative efficiency. No values for 3C 438 has been obtained.